Available online at www.sciencedirect.com
ScienceDirect
ELSEVIER
Journal of Sound and Vibration 316 (2008) 147–163
JOURNAL OF SOUND AND VIBRATION
www.elsevier.com/locate/jsvi

Long duration blade loss simulations including thermal growths for dual-rotor gas turbine engine

Guangyoung Sun[a,*], Alan Palazzolo[b,1], A. Provenza[c,2], C. Lawrence[c], K. Carney[c]

[a]NASA Glenn Research Center, 21000 Brookpark Road, MS 301-5, Cleveland, OH 44135, USA
[b]Texas A&M University, 100 ENPH Building, MS 3123, College Station, TX 77840-3123, USA
[c]NASA Glenn Research Center, Cleveland, OH 44135, USA

Received 6 December 2006; received in revised form 28 September 2007; accepted 18 February 2008
Handling Editor: S. Bolton

Abstract

This paper presents an approach for blade loss simulation including thermal growth effects for a dual-rotor gas turbine engine supported on bearing and squeeze film damper. A nonlinear ball bearing model using the Hertzian formula predicts ball contact load and stress, while a simple thermal model estimates the thermal growths of bearing components during the blade loss event. The modal truncation augmentation method combined with a proposed staggered integration scheme is verified through simulation results as an efficient tool for analyzing a flexible dual-rotor gas turbine engine dynamics with the localized nonlinearities of the bearing and damper, with the thermal growths and with a flexible casing model. The new integration scheme with enhanced modeling capability reduces the computation time by a factor of 12, while providing a variety of solutions with acceptable accuracy for durations extending over several thermal time constants.

1. Introduction

The design trend for high-performance rotating machinery such as gas turbine engines is to pursue high power output and high efficiency. It requires lighter and more flexible rotors, which may operate above bending critical speeds. Modern commercial aircraft gas turbines are usually designed as dual-rotor machines that require complex analytical models composed of two rotors rotating at different speeds and interacting through intermediate bearings. Blade loss simulations are always necessary to verify the reliability and safety of a design.

Novel squeeze film damper designs [1–3] are introduced to reduce the severe nonlinearity due to highly eccentric rotor motion during blade loss event when a squeeze film damper clearance is almost lost. A porous squeeze film damper [1], which is made of a permeable sintered porous metal material, was proposed and modeled using a rigid Jeffcott rotor for a blade loss simulation. In Refs. [2,3], a chambered porous damper

---

[*] Corresponding author. Tel.: +1 216 433 6071.
E-mail addresses: dr.gysun@gmail.com (G. Sun), a-palazzolo@neo.tamu.edu (A. Palazzolo).
[1] Tel.: +1 979 845 4580.
[2] Tel.: +1 216 433 4000.

0022-460X/$ - see front matter © 2008 Elsevier Ltd. All rights reserved.
doi:10.1016/j.jsv.2008.02.045

was designed, and blade loss experiments were conducted using a rotor operating above its first bending critical speed.

Stallone et al. [4] developed an analytical method based on the modal synthesis to predict the transient dynamic response of an aircraft engine when a fan blade is lost and they validated theoretical results with test data. Alam and Nelson [5] used a shock spectrum procedure to estimate the peak displacement response of a flexible rotor under high imbalance, however only a linear support model was used. Lawrence et al. [6] applied the pitch and yaw moments of inertias as a function of speed to consider the non-axisymmetric bladed disk and examined the effects of those moments on the rotor/disk response with a spooldown rate, and they [7] then proposed a new blade/casing interaction model and compared it with the existing contact models. Using this contact model Gallardo and Lawrence [8] derived explicit expressions of the stability boundary in terms of the whirling frequency and the required damping. Sun et al. [9] conducted blade loss transient simulations using a flexible dual-rotor engine mounted on detailed bearing and squeeze film damper models. The present research makes significant improvements of the blade loss simulation model over Ref. [9] by including the thermal effects and the staggered integration scheme as follows: (1) since the oil viscosity of squeeze film damper decreases as the viscous power loss in the oil film causes the temperature to go up, the resulting damping force is considerably decreased as the blade loss event goes on, (2) the staggered integration scheme significantly saves the computation time for blade loss simulations with local nonlinearities, while providing a variety of solutions with acceptable accuracy.

In this research, a flexible dual-rotor gas turbine engine including detailed support models is utilized for blade loss simulations. The nonlinear ball bearing model is capable of predicting the maximum contact load and stress between ball and race using Hertzian formula, while the viscous damping forces are obtained from the pressure profile in the annular oil film using finite element analysis. Furthermore, a simple thermal model estimates the thermal growths of bearing components due to rotor/rub ring friction and bearing drag torque and the resulting thermal expansions. Blade loss causes the bearings and squeeze film dampers to heat up, and the bearing clearance and the viscosity of oil film change slowly with time. The slow variation of the vibrations requires a very long total simulation time and in addition, the numerical integration time step must be kept very short because of the nonlinearities, especially the rub effect that includes an intermittently activated high stiffness. A modal truncation augmentation method combined with a staggered integration scheme provides a way to reduce the dimensionality and yet retain computational accuracy. The simulation results show that the proposed approach is an efficient tool for simulating blade loss dynamics and thermal growths over durations extending over several thermal time constants.

2. Blade loss simulation models

2.1. Dual-rotor gas turbine engine

Fig. 1 depicts a typical two-spool gas turbine engine [10]. The basic engine consists of an inner core rotor called the power turbine and an outer core rotor called the gas generator turbine, which has two stages driving an axial compressor. The power turbine rotor is supported by two main bearings located at the shaft extremities, #0 and #5, while the gas generator rotor is supported principally by rolling-element bearings at four locations: #1–#4. There are two intermediate differential bearings connecting the power turbine and gas generator rotors. The squeeze film dampers are installed at the bearing locations to provide ample viscous damping and to reduce the vibration amplitude and transmitted dynamic force.

The flexible gas turbine engine model shown in Fig. 2 is based on Ref. [10] and has a total of 38 lumped masses with the power turbine divided up into 22 nodes and the gas generator into 16 nodes. Each node has 6 degrees-of-freedom, i.e., 3 translational and 3 rotational motions, and the system has a total of 228 degrees-of-freedom. Polar moments of inertia of the rotors only at the turbine and compressor stages are considered. The gas generator rotor is connected to a flexible casing model [11] composed of the total of 118 elements with 342 degrees-of-freedom. The casing model consists of 104 solid elements (8 nodes/element, 3 degrees-of-freedom/node), 8 beam elements (2 nodes/element, 6 degrees-of-freedom) and 6 longitudinal spring-damper elements. The elements have many shared nodes in a way that the total degrees-of-freedom of the casing model are 342. The total degrees-of-freedom of the dual-rotor gas turbine engine model for the blade loss simulation are 691

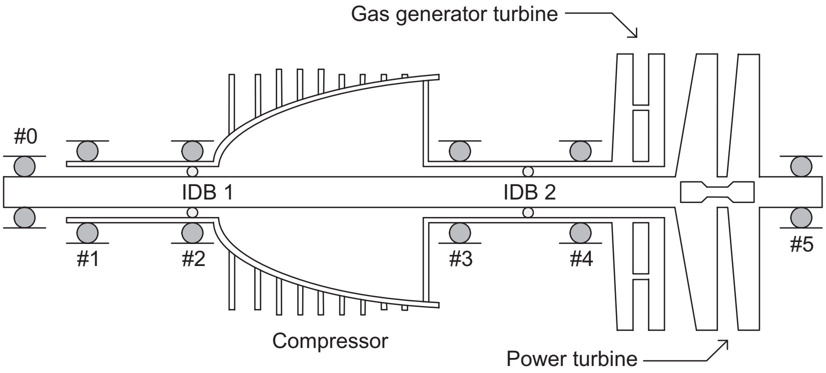

Fig. 1. Schematic two-spool gas turbine engine.

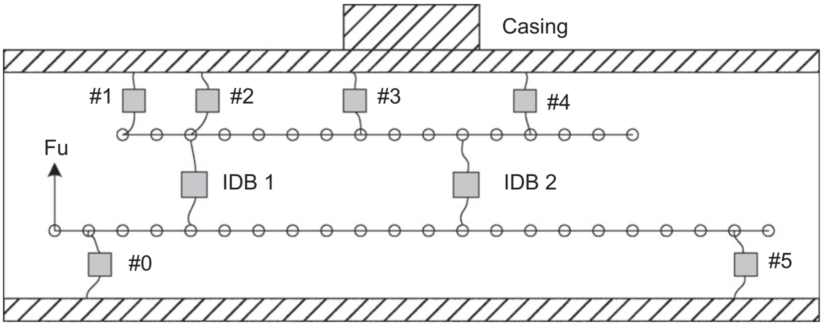

Fig. 2. Gas turbine engine model with flexible casing.

including the thermal model and the nonlinear bearing and damper models, which will be introduced in the next chapter. The arrow and F_u in Fig. 2 indicates the outboard end of the power turbine where the turbine fan blade is located and the blade loss occurs.

2.2. Nonlinear ball bearing

The bearing components are assumed to have contact only within the elastic region, and they are modeled as rigid except for local contact deformation. The angular motion is not considered here. The inner race is externally loaded by the force vector $\{F\}$ and has the displacement vector $\{X\}^{\mathrm{T}} = \{x, y, z\}$ as shown in Fig. 3(a). The $r-Z$ plane passes through the center of each ball with the angle ϕ as shown in Fig. 3(c). In Fig. 3(b), the inner race cross section at a ball is loaded by the contact force vector $\{Q\}$ at the inner race groove center p, which has a displacement vector $\{u\}$, i.e., $\{Q\}^{\mathrm{T}} = \{Q_r, Q_z\}$ and $\{u\}^{\mathrm{T}} = \{u_r, u_z\}$. The vectors for different reference points are related by a transformation matrix T:

$$\{u\} = T\{X\}, \quad \{Q\} = T\{f\}, \tag{1}$$

where

$$T = \begin{bmatrix} \cos\phi & \sin\phi & 0 \\ 0 & 0 & 1 \end{bmatrix}.$$

The vector $\{f\}$ represents an equivalent force vector at the reference coordinate. The dynamic equations of motion (eom) for the inner race are:

$$m_i\{\ddot{X}\} = \{F\} + \sum_{j=1}^{n} T_j^T \{Q\}_j, \tag{2}$$

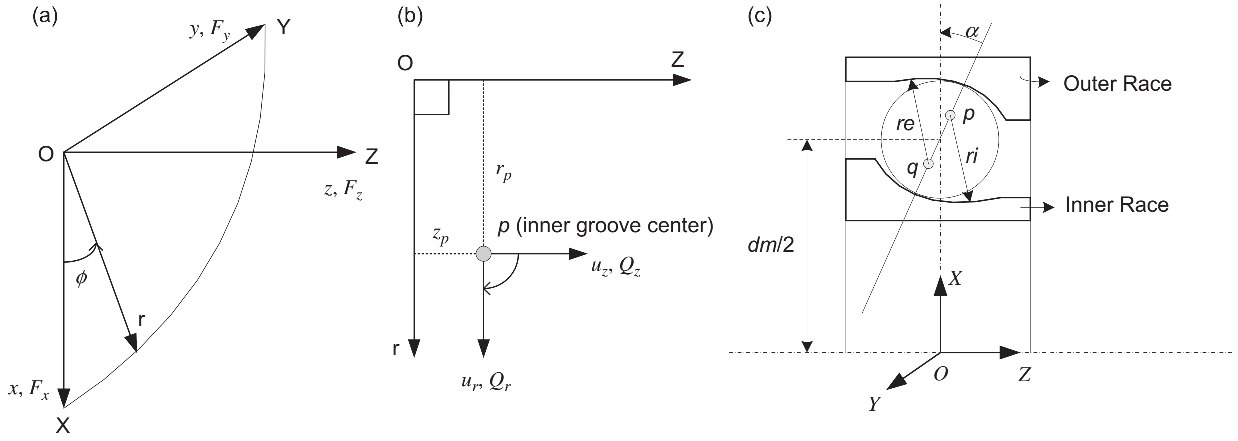

Fig. 3. (a) Bearing reference coordinate, (b) inner race groove reference center and (c) cross-sectioned ball bearing with groove centers p, q.

where n is the number of balls and m_i is the mass of inner race. The contact load vector $\{Q\}$ contributed by a ball is expressed as

$$\{Q\} = \begin{Bmatrix} Q_r \\ Q_z \end{Bmatrix} = \begin{Bmatrix} -Q_i \cos \alpha_i \\ -Q_i \sin \alpha_i \end{Bmatrix}, \tag{3}$$

where Q_i is the contact load and α_i is the contact angle between a ball and inner race.

Let the vector $\{v\}^{\mathrm{T}} = \{v_r, v_z\}$ be the displacements of a ball center. Then eom for an individual ball including centrifugal force F_c is

$$m_b \begin{Bmatrix} \ddot{v}_r \\ \ddot{v}_z \end{Bmatrix} = \begin{Bmatrix} Q_i \cos \alpha_i - Q_e \cos \alpha_e + F_c \\ Q_i \sin \alpha_i - Q_e \sin \alpha_e \end{Bmatrix}, \tag{4}$$

where the subscripts i, e represents the inner and outer races, respectively and m_b is the mass of a ball. Assuming the outer race is fitted into the squeeze film damper journal and is constrained along the axial direction, eom for the outer race in conjunction with the journal are described as

$$(m_e + m_j) \begin{Bmatrix} \ddot{x}_e \\ \ddot{y}_e \end{Bmatrix} = \begin{bmatrix} \sum_{j=1}^{n} [Q_e \cos \alpha_e]_j \cos \phi_j \\ \sum_{j=1}^{n} [Q_e \cos \alpha_e]_j \sin \phi_j \end{bmatrix} + \{F_{\mathrm{sfd}}\}, \tag{5}$$

where m_e and m_j are the masses of the outer race and the journal, respectively, and $\{F_{\mathrm{sfd}}\}$ is the damping force vector from the finite element squeeze film damper model.

Let w_r be the displacement of the outer race groove center q in the radial direction and then displacements of the groove center p and the ball center are geometrically related as in Fig. 4. The lengths l_{oi}, l_{oe} represent the distances between the ball center and the groove centers under no external force, and the lengths l_i, l_e the distances under external forces including preload. Using the geometric relation [12] between the displacements of the groove centers and ball center, the following are obtained:

$$\tan \alpha_i = \frac{l_{oi} \sin \alpha_o + u_z - v_z}{l_{oi} \cos \alpha_o + u_r + \varepsilon_i - v_r}, \quad \tan \alpha_e = \frac{l_{oe} \sin \alpha_o + v_z}{l_{oe} \cos \alpha_o + v_r - w_r - \varepsilon_e}, \tag{6}$$

$$l_i = \varepsilon_b + \sqrt{(l_{oi} \cos \alpha_o + u_r + \varepsilon_i - v_r)^2 + (l_{oi} \sin \alpha_o + u_z - v_z)^2}, \tag{7}$$

$$l_e = \varepsilon_b + \sqrt{(l_{oe} \cos \alpha_o + v_r - w_r - \varepsilon_e)^2 + (l_{oe} \sin \alpha_o + v_z)^2},$$

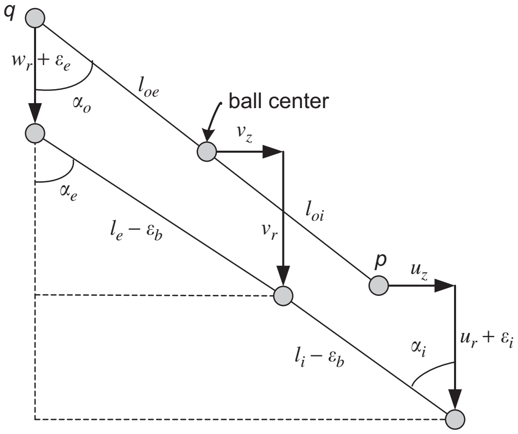

Fig. 4. Displacements of ball, inner race and outer race.

where ε indicates the thermal expansion of a bearing component. The relative deflections δ at the contacts are then

$$\delta_i = l_i - l_{oi}, \quad \delta_e = l_e - l_{oe}. \tag{8}$$

The point contact forces [13] are obtained from the Hertzian formula:

$$Q_i = k_i \delta_i^{3/2}\left(\frac{3}{2}\alpha\dot{\delta}_i + 1\right), \quad Q_e = k_e \delta_e^{3/2}\left(\frac{3}{2}\alpha\dot{\delta}_e + 1\right), \tag{9}$$

where α is linearly related to the coefficient of restitution of materials engaged in contact and has a value ranging from 0.08 to 0.32 s/m for steel and bronze. The ball contact stress [13] at the center of an elliptical contact area is calculated as

$$\sigma_{i,e} = -\frac{3Q_{i,e}}{2\pi a_{i,e} b_{i,e}}, \tag{10}$$

where a, b are the semimajor and semiminor axes of the projected elliptical area and the minus sign indicates compression.

2.3. Bearing thermal model

A ball bearing has a variety of heat sources, however two major sources were considered here during the blade loss event: rotor/rub ring friction and bearing drag torque. The bearing drag torque is contributed by bearing type, external load, lubricant and operating speed, and the empirical formula is available in Ref. [13].

The rub ring, which is usually located closely to the support bearings, protects the system from being damaged by an excessive vibration due to rotor imbalance. When the rotor whirl amplitude at the bearing exceed the rub ring clearance, the power loss due to the rotor/rub ring contact is expressed as

$$H_s = F_f(R_r \omega_r), \tag{11}$$

where F_f is the friction force due to the mechanical rub, and R_r and ω_r are the radius and the rotor speed, respectively.

Jorgensen and Shin [14] proposed a bearing thermal model for high-speed milling machine, and Sun [12] a thermal model for auxiliary bearings of an energy-storage flywheel system. Based on their model, a bearing thermal model is developed assuming the heat flux to the radial direction is uniform. Fig. 5(a) shows a cross-sectioned support bearing with thermal nodes and Fig. 5(b) the heat transfer network, which consists of

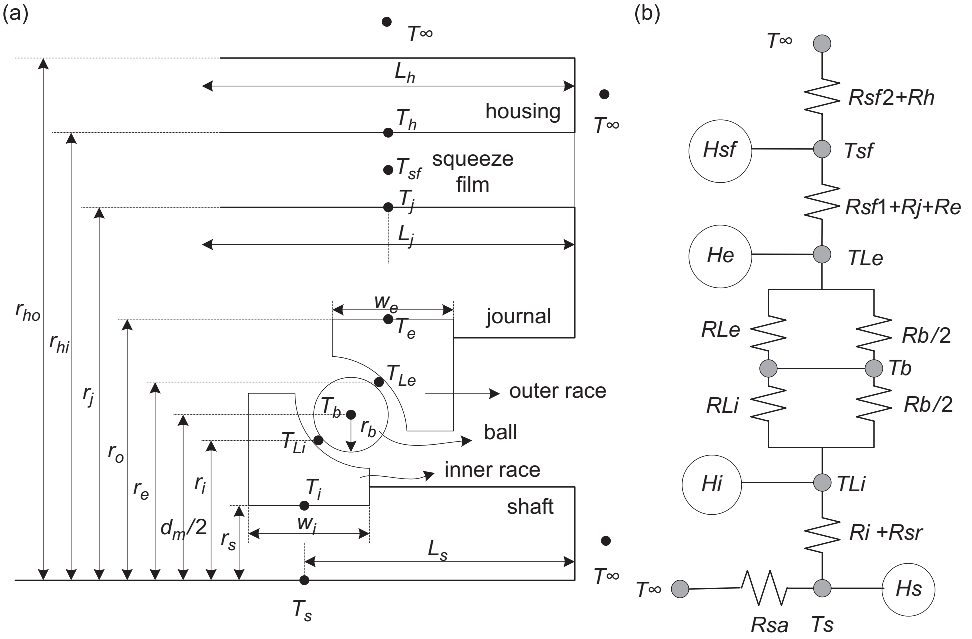

Fig. 5. (a) Cross section of ball bearing with thermal nodes and (b) heat transfer network.

Table 1
List of thermal resistances in heat transfer network

Ball/lubricant	Inner race/shaft	Outer race/journal
$R_{\mathrm{Li}} \approx \dfrac{r_b}{k_l(2\pi r_i W_i - \pi n r_b^2)}$	$R_i = \dfrac{\ln(r_i/r_s)}{2\pi k_i W_i}$	$R_e = \dfrac{\ln(r_o/r_e)}{2\pi k_e W_e}$
$R_{\mathrm{Le}} \approx \dfrac{r_b}{k_l(2\pi r_e W_e - \pi n r_b^2)}$	$R_{sr} = \dfrac{1}{\pi k_s W_i}$	$R_j = \dfrac{\ln(r_j/r_o)}{2\pi k_j W_e}$
$R_b \approx \frac{1}{n k_b \pi r_b}$	$R_{sa} = \dfrac{L_s}{k_s \pi r_s^2} + \dfrac{1}{h_s \pi r_s^2}$	$R_h = \dfrac{R_{hr} R_{ha}}{R_{hr} + R_{ha}}$
Squeeze film damper	Housing	
$R_{sf1} = \dfrac{\ln((r_j + c_{sf}/2)/r_j)}{2\pi k_{sf} L_j}$	$R_{hr} = \dfrac{\ln(r_h/r_o)}{2\pi k_h L_h} + \dfrac{1}{h_h 2\pi r_h L_h}$	
$R_{sf2} = \dfrac{\ln(r_{hi}/(r_j + c_{sf}/2))}{2\pi k_{sf} L_j}$	$R_{ha} = \dfrac{L_h}{2\pi k_h (r_h^2 - r_o^2)} + \dfrac{1}{\pi h_h (r_h^2 - r_o^2)}$	

thermal resistances, heat masses and heat sources. The thermal resistances are a function of geometric and material properties, and they are listed in Table 1. The following first-order thermal equation is then developed for each node:

$$m_h C_p \, \mathrm{d}T/\mathrm{d}t = Q_i - Q_o, \tag{12}$$

where m_h is a lumped heat mass, C_p is the specific heat, and $Q_{i,o}$ are the heat flux in and out, respectively.

Assuming a linear temperature distribution the thermal expansion ε_e [15] of the outer race combined with the squeeze film damper journal is given by

$$\varepsilon_e = \frac{\xi_e}{3}\frac{(1+v_e)r_e}{r_e+r_j}[\Delta T_{\mathrm{Le}}(2r_e+r_j)+\Delta T_j(2r_j+r_e)], \tag{13}$$

where ξ_e [m/m °C] is the thermal expansion coefficient of the outer race, v_e the Poisson's ratio and ΔT the temperature change from an initial value. Similarly, the thermal expansion of the inner race and shaft is determined from

$$\varepsilon_i = \frac{\xi_i}{3}(\Delta T_s + \Delta T_{\mathrm{Li}})(1+v_i)r_i. \tag{14}$$

The thermal expansion of a ball with uniform temperature distribution is

$$\varepsilon_b = \xi_b r_b \Delta T_b, \tag{15}$$

where r_b is the ball radius. The thermal expansions of the bearing components are then substituted into the Hertzian ball contact loads, Eqs. (9) and (10).

3. Modal analysis combined with staggered integration scheme

3.1. Modal truncation augmentation method

The response of a structure can be evaluated using the modal response method, which is a relatively simple and well-established method. This method reduces the model into a much smaller number of dynamic degrees-of-freedom. Unfortunately, this reduction process alters the modal representation of the applied loading and can adversely affect the quality of the results. This can be overcome by representing the truncated modal response using either the mode acceleration [16] or the modal truncation augmentation [17]. Dickens et al. [18] have compared these two methods both theoretically and numerically, and have concluded that the modal truncation augmentation method is superior to the mode acceleration method in that the mode acceleration method is a special case of the modal truncation augmentation method and the modal truncation augmentation results are more accurate.

Dynamics equation for a linear structural system is described as

$$[M]\{\ddot{q}(t)\} + [C]\{\dot{q}(t)\} + [K]\{q(t)\} = \{F(t)\} = \{F_o\}g(t). \tag{16}$$

The load vector $\{F(t)\}$ can be divided into two parts: $\{F_o\}$ is the invariant spatial portion and $g(t)$ the time varying portion. The load vector may be composed of several invariant portions. The eigenvalue problem is given by

$$[K][\Phi] = [M][\Phi]\underline{\omega^2}, \tag{17}$$

where $[\Phi]$ is the matrix of retained eigenmodes and $\underline{\omega^2}$ represents a diagonal matrix of the squares of all retained mode natural frequencies.

A force truncation vector $\{F_t\}$ is defined to be the portion of the load vector that is not represented by the retained modes which are far fewer than the total system modes. It is given by

$$\{F_t\} = \{F_o\} - \{F_s\}, \tag{18}$$

The modally represented spatial load vector $\{F_s\}$ is derived as $\{F_s\} = [M][\Phi][\Phi]^{\mathrm{T}}\{F_o\}$ [11]. Since the force truncation vector represents the portion that is lost due to modal truncation, it has to be reduced to improve the accuracy of response. Then, form

$$\begin{aligned}\overline{[K]} &= [X]^{\mathrm{T}}[K][X],\\ \overline{[M]} &= [X]^{\mathrm{T}}[M][X],\end{aligned} \tag{19}$$

where $[X]$ is a matrix of column vectors $\{X\}_i$, each representing the static response of the system to an equivalent static load vector $\{F_t\}_i$, i.e., $[K]\{X\}_i = \{F_t\}_i$. Then, solve the reduced eigenvalue problem as $\overline{[K]}[\psi] = \overline{[M]}[\psi][\varpi]$. The modal truncation vector $\{\eta\}$ can now be formed as $\{\eta\} = \{X\}[\psi]$. The modal truncation vector is appended to the retained modal set to construct the pseudo-modal set: $[\tilde{\Phi}] = [\,\Phi \quad \eta\,]$. This modal set is used to transform the physical coordinates into the modal coordinates as

$$\begin{aligned}\{q(t)\} &= [\tilde{\Phi}]\{\chi(t)\},\\ \{\dot{q}(t)\} &= [\tilde{\Phi}]\{\dot{\chi}(t)\},\\ \{\ddot{q}(t)\} &= [\tilde{\Phi}]\{\ddot{\chi}(t)\}.\end{aligned} \tag{20}$$

Substituting Eq. (20) into Eq. (16), the augmented modal equation is

$$[\tilde{M}]\{\ddot{\chi}(t)\} + [\tilde{C}]\{\dot{\chi}(t)\} + [\tilde{K}]\{\chi(t)\} = \{\tilde{F}(t)\}, \tag{21}$$

where

$$\begin{aligned}[\tilde{M}] &= [\tilde{\Phi}]^{\mathrm{T}}[M][\tilde{\Phi}],\\ [\tilde{C}] &= [\tilde{\Phi}]^{\mathrm{T}}[C][\tilde{\Phi}],\\ [\tilde{K}] &= [\tilde{\Phi}]^{\mathrm{T}}[K][\tilde{\Phi}],\\ \{\tilde{F}(t)\} &= [\tilde{\Phi}]^{\mathrm{T}}\{F(t)\}.\end{aligned} \tag{22}$$

After completing the modal response analysis, the physical acceleration, velocity and displacements are calculated using Eq. (20).

3.2. Staggered integration scheme

A staggered integration scheme [12] is proposed to greatly increase the computational efficiency without losing the accuracy of solutions for a dynamic model, which has local nonlinearities and two types of solutions with different time constants. The blade loss simulation with thermal growth is carried out using the modal truncation augmentation method combined with the staggered integration scheme intermittently with a thermal-only integration interval between thermo-mechanical intervals. A thermal-only interval is defined to be one, during which only the bearing thermal equations are integrated with a relatively large time step and constant power sources calculated during the previous thermal-mechanical interval. A thermal-mechanical interval is defined to be one during which the complete dual-rotor dynamic equations and the bearing thermal equations are integrated simultaneously with a relatively small time step. The integration technique is based on the assumption that once the mechanical steady state is reached, there is no significant change in the dynamic response. A power loss of the root-mean-square type is calculated for the last 5 cycles of a thermal-mechanical interval and applied to the next thermal-mechanical interval as the heat source. After the completion of the thermal-only interval integration, the final temperatures are used as the initial condition of the next thermal-mechanical interval. This process can be used alternately several times to obtain extended simulation results. The duration of each interval is decided on a trial and error basis.

4. Simulation results and discussion

4.1. Long duration blade loss simulations

Blade loss simulations are conducted to illustrate the efficiency of the modal truncation augmentation method combined with the staggered integration scheme and the implementation of the flexible dual-rotor gas turbine engine in the flexible casing supported on the nonlinear ball bearings and dampers. The Newmark Beta method [19] is utilized to perform the numerical integration. Only the support bearings #0 and #5 of the power turbine rotor are modeled as the nonlinear bearings, and the four bearings of the gas generator and two intermediate differential bearings are modeled as a linear support system shown in Table 2. The dimensional and material specifications for the bearings #0 and #5 and the squeeze film damper are listed in Table 3.

Fig. 6 shows a schematic drawing of the blade loss simulation model. The flexible two rotors are interacted by the two linear bearings. The flexible power turbine rotor is connected to the nonlinear bearings by exchanging the rotor displacement and velocity vectors X and $\dot{X}$ into the nonlinear bearing force $F_{\mathrm{n\_brg}}$. The

Table 2
Stiffness and damping of support system

Bearing number	Stiffness (N/m) × 10^{-8}	Damping (N s/m) × 10^{-3}
1	1.751	1.751
2	1.751	1.751
3	0.876	1.751
4	0.701	1.751
Intermediate differential bearing	0.875	3.502

Table 3
Specifications of detailed bearing and damper

Dimension	Bearing #0	Bearing #5
Geometry		
Bore diameter, BD	5.08 (cm)	8.38
Outside diameter, OD	9 (cm)	11
Width	2 (cm)	1.6
Number of balls	21	27
Diameter of a ball	8.73 (mm)	9.53
Initial contact angle	15 (deg)	15
Axial preload	800 (N)	1100 (N)
Number of rows	1	1
Material		
Density of ball: steel	7.8 (g/cm^3)	7.8
Density of race: steel	7.8 (g/cm^3)	7.8
Elastic modulus of ball	208 (GPa)	208
Poisson's ratio of ball	0.3	0.3
Elastic modulus of race	208 (GPa)	208
Poisson's ratio of race	0.3	0.3
Support system		
Stiffness of o-ring	5254 (N/mm)	5254
Squeeze film damper journal radius	8 (cm)	10
Squeeze film damper journal length	3.2 (cm)	4
Oil viscosity, SAE 30	92 (cP) at 40 °C, 11 at 100 °C	
Supply pressure	0.2 MPa	0.2
Squeeze film damper radial clearance	0.635 (mm)	0.635
Rub ring clearance	0.508 (mm)	0.508

nonlinear bearing model provides the journal motion $x_j, \dot{x}_j$ to the finite element squeeze film damper and receives the viscous damping force from the finite element squeeze film damper in return. The bearing thermal model calculates the thermal growths of the bearing components and the squeeze film damper oil film using the power loss (PL). The bearing drag torque and the viscous dissipation in squeeze film damper are the main PL in the thermal model. However, when the power turbine rotor makes contact with the rub rings the mechanical power loss due to the friction is generated and it significantly influences the thermal growths and the vibrations.

Fig. 7 shows the geometry, the finite element mesh and boundary conditions of the squeeze film damper model [12]. Only the half journal is used assuming that the pressure profile is symmetric with respect to the axial center of journal and the flow rate across the vertical plane cutting the axial center is zero, i.e., $q_n = 0$ along $\tilde{Y} = L_j/2$ in Fig. 7(b). The supply pressure P_s is applied to the journal ends. Using a simple triangular element the total 128×64 FEs are used to calculate the pressure profile and the resulting damping force.

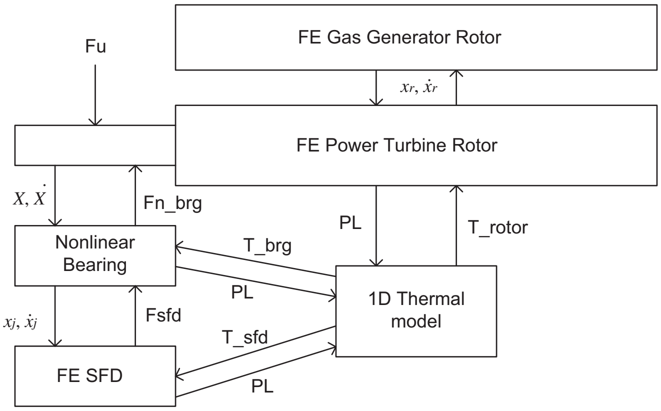

Fig. 6. Blade loss simulation model with input–output connections.

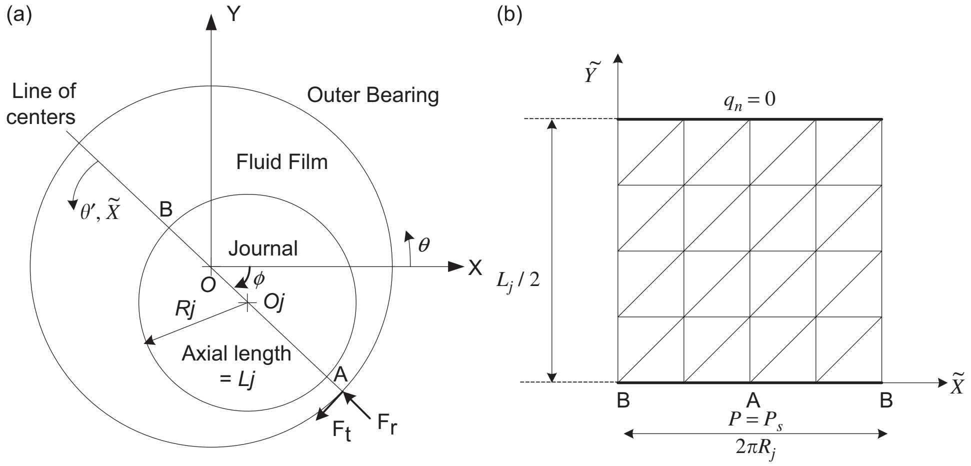

Fig. 7. (a) Geometry and (b) mesh and boundary conditions of squeeze film damper model.

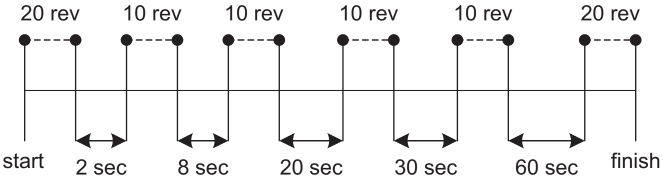

Fig. 8. Two minute blade loss simulation time line: thermo-mechanical, rev.; thermal-only, sec.

The power turbine and gas generator rotors are rotating at 16,000 and 15,000 rev/min, respectively. The running speeds are constant during the simulation. The lowest two forward, synchronous critical speeds are calculated to be 8500 rev/min and 10,200 rev/min. Several revolutions of time response under low imbalance are simulated to obtain a steady-state dynamic response prior to the blade loss event. A sudden imbalance force due to the turbine fan blade loss is then applied at the outboard end of the power turbine rotor at the simulation time 0.01 s. The applied amount of force due to blade loss varies from 712 to 14,252 N depending on the severity. Initial temperature of the bearing components and ambient temperature are set to at 30 °C.

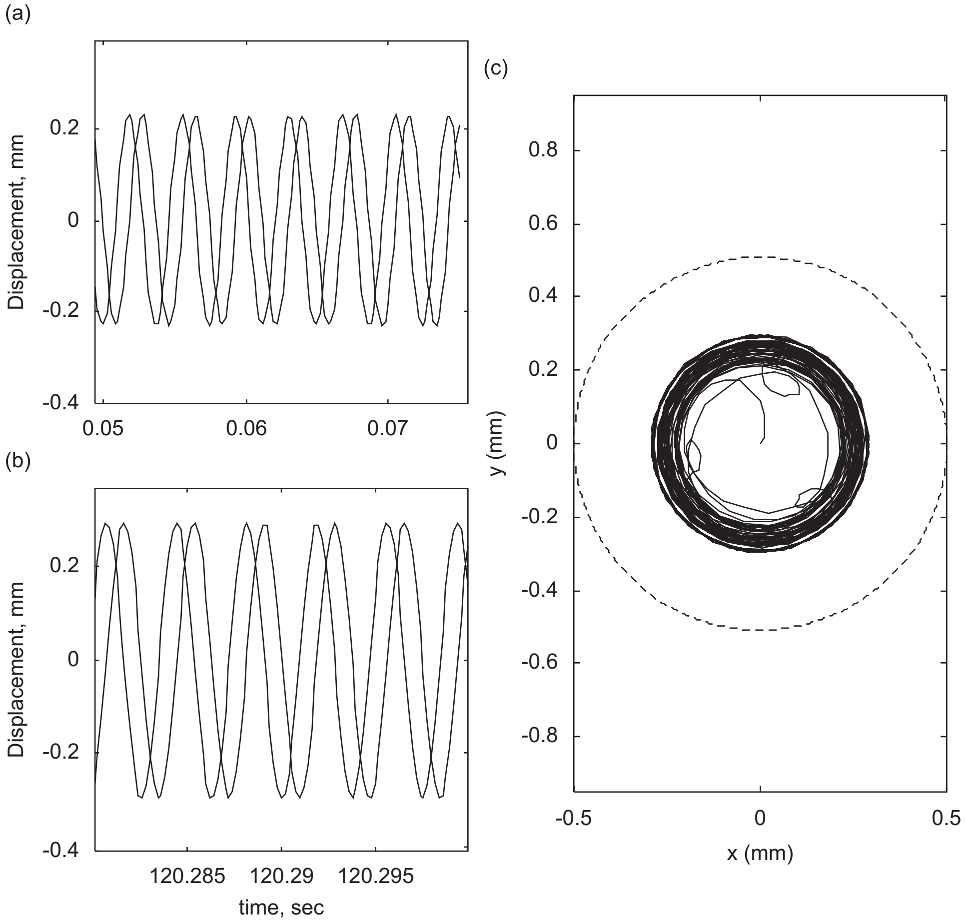

Fig. 9. (a) Transient and (b) steady-state responses: solid, x-axis; dotted, y-axis and (c) orbit plot of power turbine rotor at bearing #0.

The integration time step for the thermal-only interval is set to 1 ms to estimate ball contact load and stress during the blade loss, while that for the thermal-only interval is set to 0.1 s. Fig. 8 shows a 2 min simulation time line composed of the 6 thermal-only and the 5 thermal-only intervals.

From Figs. 9 to 14 are provided the simulation results for the unbalance force of 2850 N. Fig. 9 shows the dynamic response and orbit plot of the power turbine rotor at the bearing #0, while Fig. 10 shows those at the bearing #5. The dotted circle in Fig. 9(c) indicates the rub ring clearance of 0.508 mm. The whirl amplitude at the bearing #0 reaches about 0.2 mm and that at the bearing #5 less than 0.01 mm after a short period of the transient response. The whirl amplitude at the bearing #0 noticeably increases from the transient amplitude 0.2 mm in Fig. 9(a) up to about 0.3 mm in Fig. 9(b) because of the viscosity drop of squeeze film damper due to thermal growths. Meanwhile the whirl amplitude at the bearing #5 barely increases.

The transmissibility at a bearing is defined to be

$$T = \frac{|F_{\mathrm{sfd}} + F_{\mathrm{cs}}|}{|F_u|}, \tag{23}$$

where F_u is the unbalance force induced by blade loss, F_{sfd} is the squeeze film damper force and F_{cs} is the centering spring force. Fig. 11 shows that the steady-state transmissibility at the bearing #0 reaches around 1.25 and that at the bearing #5 is less than 0.04 at the end of simulation. The transmissibility at the bearing #0 barely changes with the given unbalance force during the 2 min simulation. Fig. 12 shows the maximum contact stress between the outer race and ball at each time step. As expected, the contact stress at the bearing

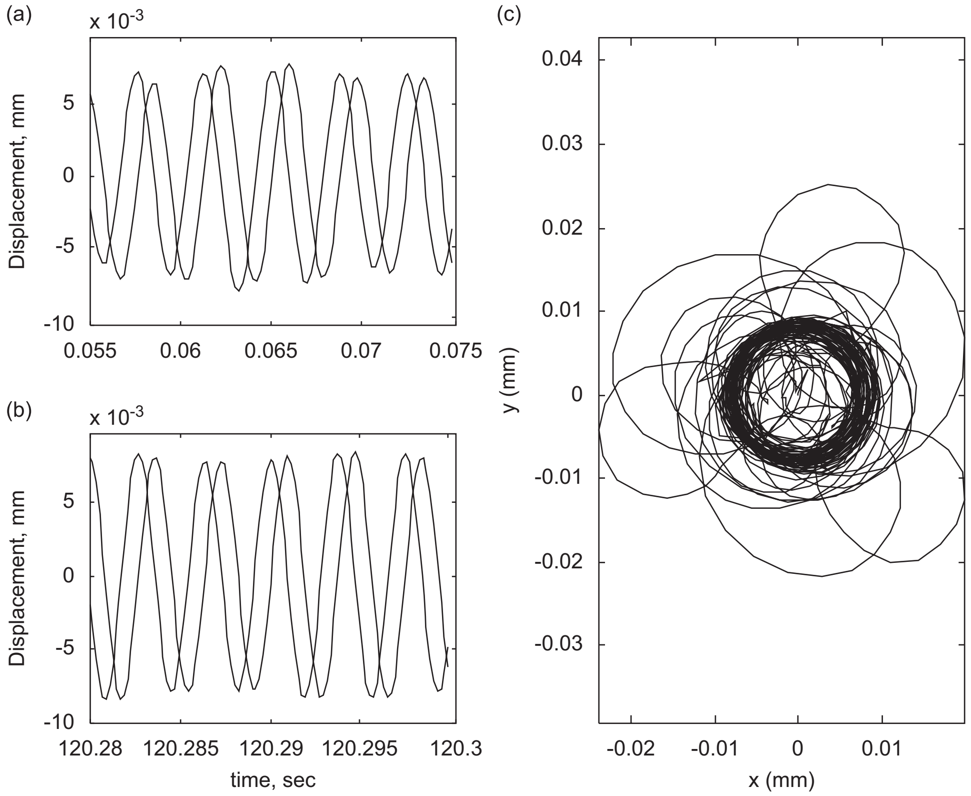

Fig. 10. (a) Transient and (b) steady-state responses: solid, *x*-axis; dotted, *y*-axis and (c) orbit plot of power turbine rotor at bearing #5.

#0 where the fan blade loss occurs is much higher than that at the bearing #5. The transient state with high frequency and high amplitude just after the blade loss is observed, but soon it is damped out. As shown in Fig. 12(b), the transition from the thermal-only to thermal-mechanical interval introduces the transient vibration, however it goes away soon. The contact stress is used as an index for permanent damage on the ball/race contact area initiating at 3200 MPa. Figs. 13 and 14 show the thermal growths of the bearing components and the squeeze film damper oil. Since the drag torque of bearing #5 is greater than that of bearing #0 and there was not any mechanical contact of rotor and rub ring, the temperatures of the bearing #5 become higher than those of the bearing #0. It is also noticed that since the squeeze film damper oil heats up by the journal motion the oil temperature of the bearing #0 is 18 °C higher than that of the bearing #5 is at the end of simulation.

Table 4 shows the 11 result categories selected to compare the simulation results, and their outcomes induced by the unbalance amount are summarized in Table 5. The rotor/rub ring contact does not occur below the imbalance force of 2850 N. The steady-state mechanical power loss of 18,990 W due to the rotor/rub ring contact occurs at the unbalance case of 5700 N, which contributes to the drastic thermal increases of the bearing #0. The final temperatures as well as the power loss of the bearing #0 increase continuously with the imbalance level beyond this amount.

Note that the temperatures of each component of the bearing #5 are similar regardless of the applied imbalance amount and they are higher than those of the bearing #0 except for the squeeze film damper oil before the rotor/rub ring contact occurs because the bearing #5 generates higher drag torque, however those of the bearing #0 drastically increase after the rotor whirl amplitude exceeds the rub ring clearance 0.508 mm because the power loss due to the friction becomes the major heat source. The final temperature of the inner race of the bearing #0 increases approximately up to 200 °C in the largest-imbalance case. The ball contact

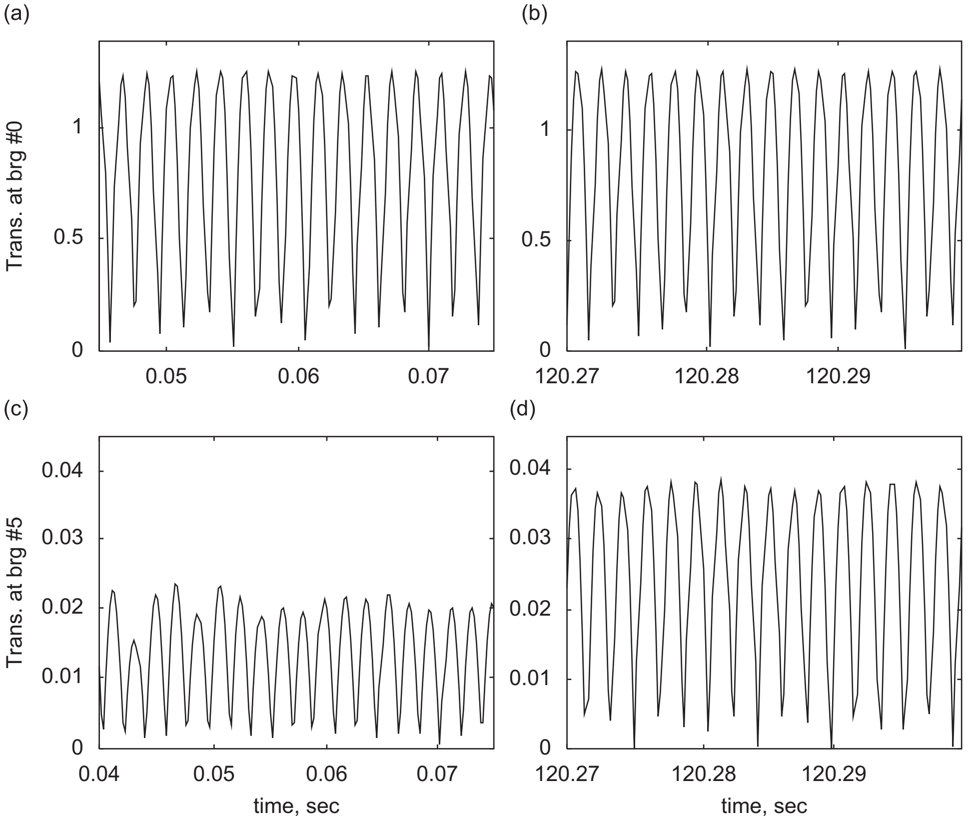

Fig. 11. (a) Transient and (b) steady-state transmissibility at bearing #0 and (c) transient and (d) steady-state transmissibility at bearing #5.

stresses at the last two imbalance cases reach the incipient plastic flow limit 3200 MPa [13], which initiates permanent strains on the ball/race contact area. When the permanent strain is initiated on a ball or a race inside the ball bearing, the bearing starts making an excessive vibration and noise, and the initial damage due to the permanent strain is further developed because the bearing is a high-precision machine element rotating at high speed. The maximum contact stress would have been much higher unless the rub ring was installed.

4.2. *Efficiency of staggered integration scheme*

In order to verify the computational efficiency including accuracy of the proposed integration scheme, the simulations results at the bearing #0 with the imbalance force of 2850 N are used to compare the cases with and without the staggered integration scheme. The total simulation time is set to 2 s. The case without the staggered integration scheme uses the time step of 1 ms during the entire simulation, while the case with the staggered integration scheme adopts 3 thermal-only intervals (50 rev) with the time step of 1 ms and 2 thermal-only intervals (1.815 s) with the time step of 0.1 s.

Table 6 shows the comparison of the results at the end of simulation. The dynamic response, the ball contact load and stress, the power loss, and the final temperatures of the bearing components show less than 5% relative errors (Er), while the computation time is improved by a factor of 12 by using the proposed integration scheme. Therefore the proposed staggered integration scheme is verified as an efficient tool for obtaining and analyzing time integrated solutions of the gas turbine engine blade loss dynamics with thermal growths and nonlinear multi-bodies dynamics support models.

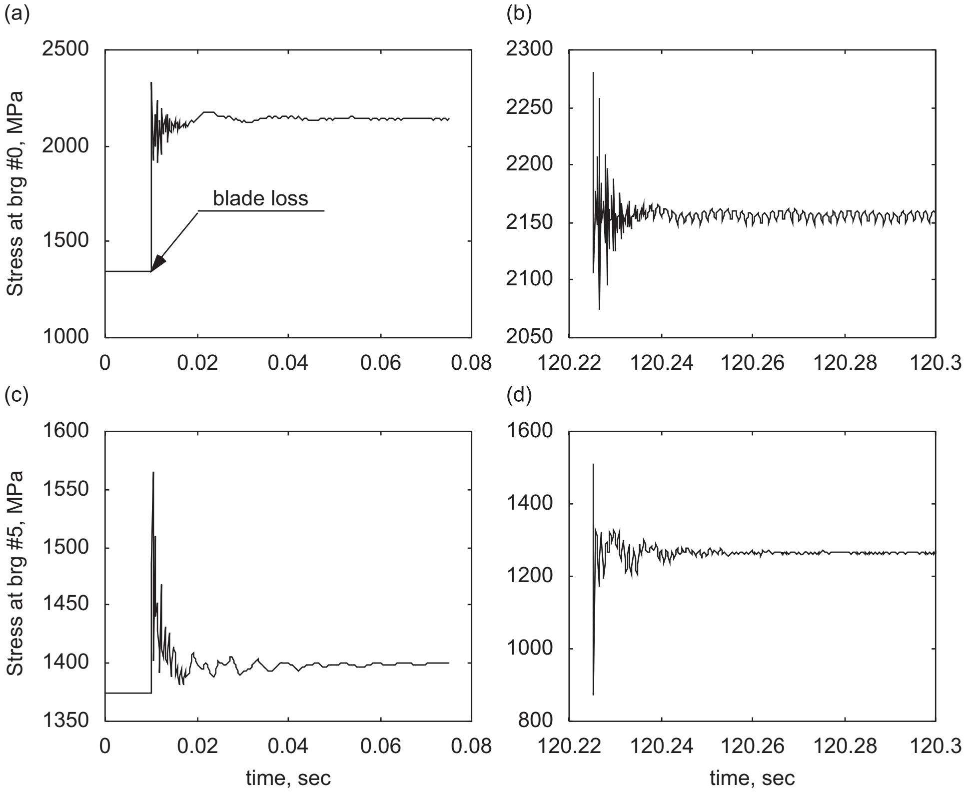

Fig. 12. (a) Transient and (b) steady-state contact stress at bearing #0 and (c) transient and (d) steady-state contact stress at bearing #5.

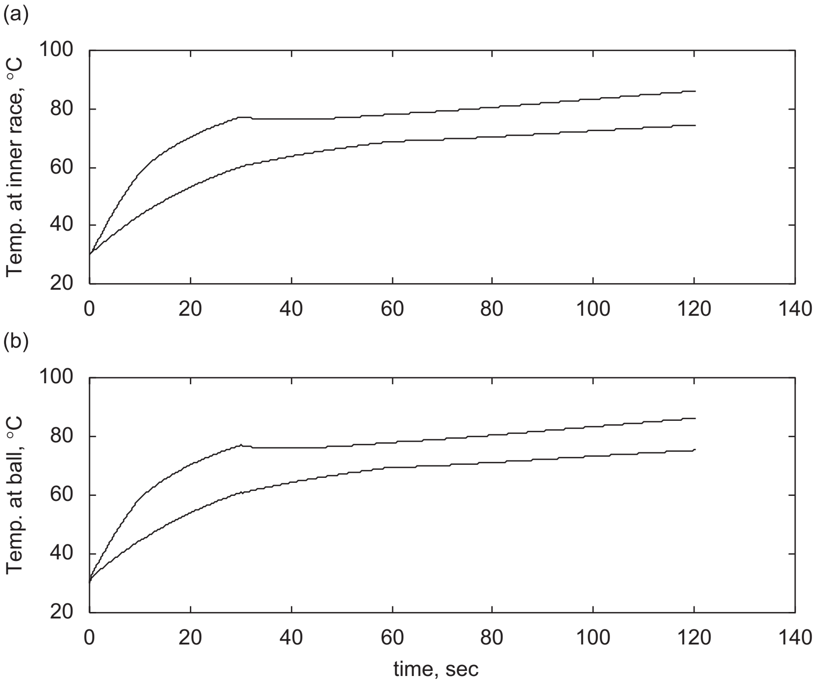

Fig. 13. Thermal growths (a) at inner race and (b) at ball: solid, bearing #0; dotted, bearing #5.

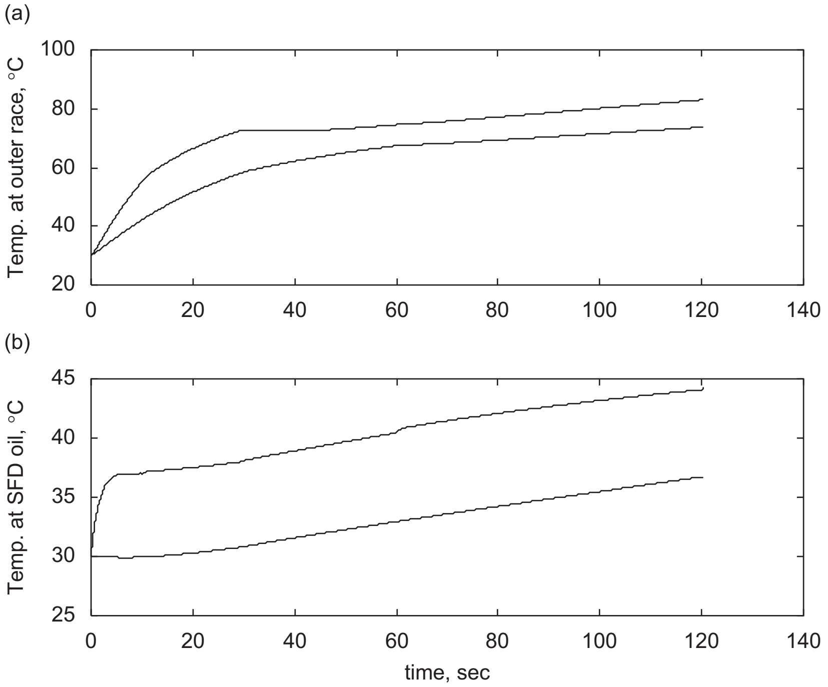

Fig. 14. Thermal growths (a) at outer race and (b) at squeeze film damper oil: solid, bearing #0; dotted, bearing #5.

Table 4
Simulation results for comparison

No	Title
Result 1 (mm)	Steady-state whirl amplitude
Result 2	Transmissibility
Result 3 (N)	Maximum contact load
Result 4 (MPa)	Maximum contact stress
Result 5 (W)	Power loss due to rotor/rub ring contact
Result 6 (W)	Power loss due to drag torque
Result 7 (W)	Power loss due to viscous dissipation of squeeze film damper
Result 8 (°C)	Final temperature of inner race
Result 9 (°C)	Final temperature of ball
Result 10 (°C)	Final temperature of outer race
Result 11 (°C)	Final temperature of squeeze film damper oil

5. Conclusions

In this paper is developed an efficient and accurate approach for simulating blade loss effects on vibrations and thermal growths for a dual-rotor gas turbine engine utilizing the modal truncation augmentation combined with the staggered integration scheme, which greatly increases the computational efficiency without significantly penalizing and enables a 2 min blade loss simulation. The nonlinear bearing model estimates the ball contact load and stress and the thermal expansions of the components during blade loss, and the squeeze film damper model calculates the nonlinear damping force from an oil pressure profile using FEM. The one-dimensional bearing thermal model predicts the thermal growths of the bearing components due to the rotor/rub ring contact, the bearing drag torque and the viscous power loss in the squeeze film damper. Including the thermal effects improves the blade loss simulation model in that since the oil viscosity of squeeze

Table 5
Summary of blade loss simulation results

Unbalance, *N*	712	1425	2850	5700	8551	11,401	14,252
Result 1 (mm)							
Brg #0	0.0512	0.1046	0.2958	0.5438	0.5652	0.6795	0.7087
Brg #5	0.004	0.0032	0.0084	0.0112	0.0104	0.0153	0.0114
Result 2							
Brg #0	1.03	1.02	1.27	1.62	1.21	1.05	1.21
Brg #5	0	0.044	0.038	0.023	0.014	0.0096	0.0075
Result 3 (N)							
Brg #0	198.85	352.7	658.6	972.2	1351.5	2073.4	2252.5
Brg #5	100.97	137.85	158.45	168.86	164.6	310.7	436.6
Result 4 (MPa)							
Brg #0	1449.6	1754.8	2161	2460.4	2745.8	3167.1	3255.5
Brg #5	1092.7	1212.1	1269.7	1290.1	1286	1589.4	1780
Result 5 (W)							
Brg #0	0	0	0	18,990	31,960	105,860	128,690
Brg #5	0	0	0	0	0	0	0
Result 6 (W)							
Brg #0	348.3	354.07	368.1	349.2	337.3	359.6	424.1
Brg #5	622.9	623.96	624.6	624.7	624.7	625.7	624.6
Result 7 (W)							
Brg #0	30.56	124.45	638.81	1924.55	2079.6	2221.7	2806.4
Brg #5	0	0.32	0.95	1.33	1.2	1.72	1.26
Result 8 (°C)							
Brg #0	68.2	69.5	74.4	115.2	145.1	171.7	197.1
Brg #5	86.1	86.1	86.1	86.2	86.2	86.1	86.2
Result 9 (°C)							
Brg #0	68.9	70.3	75.4	114.1	141.5	165.8	191.7
Brg #5	86.2	86.2	86.3	86.3	86.3	86.3	86.3
Result 10 (°C)							
Brg #0	67.1	68.41	73.7	110.2	135.2	157.5	182.9
Brg #5	83	83	83.0	83.1	83.1	83.1	83.1
Result 11 (°C)							
Brg #0	33.0	34.8	44.3	75.1	83	90	123.3
Brg #5	36.7	36.7	36.7	36.7	36.7	36.7	36.8

Table 6
Comparison of simulation results with and without staggered integration scheme (Intel P. III 1 GHz Microprocessor)

Results	*w*	*w/o*	Er (%)
Result 1 (mm)	0.2574	0.2656	3.1
Result 2	1.258	1.26	0.3
Result 3 (N)	619.8	615.4	0.7
Result 4 (MPa)	2117.8	2112.6	0.25
Result 6 (W)	599.85	596.7	0.5
Result 7 (W)	587.7	592	0.7
Result 8 (°C)	33.2	33.5	0.9
Result 9 (°C)	35.1	35.5	1.2
Result 10 (°C)	32.7	32.9	0.6
Result 11 (°C)	36.9	37.7	2.1
Comp. time (h)	3.5	43.9	N/A

film damper fully depends on the temperature, the damping force drop for a long duration is explained through the proposed simulation model.

Major power loss due to the power turbine rotor/rub ring contact was generated above the imbalance force of 5700 N, which contributed to the abrupt thermal increase of the bearing components. The inner race temperature of the bearing #0 reached approximately 200 °C, and the squeeze film damper oil temperature increased to 123 °C in the largest-imbalance case. The ball contact stresses in the two largest-imbalance cases nearly exceeded the incipient plastic flow limit 3200 MPa, which resulted in the permanent strains on the contact surface of ball and races.

The comparison of the simulation results with and without the staggered integration scheme showed that the proposed modal truncation augmentation in conjunction with staggered integration scheme greatly reduced the computation time by a factor of 12, while providing a variety of simulation results and maintaining the simulation relative errors less than 5%.

For future work, the current simulation model will be enhanced to include the deceleration torque and the high-temperature magnetic bearings, which provide active vibration control.

Acknowledgments

The authors gratefully acknowledge support of this research on NASA Glenn grants NRA-GRC-99-02 and National Research Council grants 2005.

References

[1] S. Zhang, L. Yan, Q. Li., Development of porous squeeze film damper bearings for improving the blade loss dynamics of rotor-support systems, *Journal of Vibration and Acoustics* 114 (1992) 347–353.

[2] J. Tecza, J. Walton, A chambered porous damper for rotor vibration control: part I—concept development, *Journal of Engineering for Gas Turbines and Power* 115 (1993) 360–365.

[3] J. Walton, M. Martin, A chambered porous damper for rotor vibration control: part II—imbalance response and blade loss simulation, *Journal of Engineering for Gas Turbine and Power* 115 (1993) 366–371.

[4] M.J. Stallone, V. Gallardo, A.F. Storace, L.J. Bach, G. Black, Blade loss for transient dynamic analysis of turbomachinery, *AIAA Journal* 21 (1983) 1134–1138.

[5] M. Alam, H.D. Nelson, A blade loss response spectrum for flexible rotor systems, *Journal of Engineering for Gas Turbines and Power* 107 (1985) 197–204.

[6] C. Lawrence, K. Carney, V. Gallardo, Simulation of aircraft engine blade-out structural dynamics, NASA/TM-2001-210957/REV1, 2001.

[7] C. Lawrence, K. Carney, V. Gallardo, A study of fan/casing interaction models, NASA/TM-2003-21215, 2003.

[8] V. Gallardo, C. Lawrence, Turbine engine stability/instability with rub forces axisymmetric rotor-support stiffness, NASA/TM-2004-212974, 2004.

[9] G. Sun, N. Kaushik, A.B. Palazzolo, A.J. Provenza, C. Lawrence, K. Carney, An efficient algorithm for blade loss simulations using a high fidelity ball bearing and damper model, *American Society of Mechanical Engineering 19th Biennial Conference on Mechanical Vibration and Noise*, Chicago, USA, September 2003, DETC 2003/VIB 48424.

[10] D. Li, Dynamic Analysis of Complex Multi-level Flexible Rotor Systems, PhD Dissertation, University of Virginia, 1978.

[11] N.K. Parthasarathy, An Efficient Algorithm for Blade Loss Simulation Applied to a High-order Rotordymanics Problem, MS Thesis, Texas A&M University, 2003.

[12] Guangyoung Sun, A High Fidelity Ball Bearing and Damper Model Including Thermal Effects for Magnetic Suspension Auxiliary Service and Blade Loss Simulation, PhD Dissertation, Texas A&M University, 2003.

[13] T.A. Harris, *Rolling Bearing Analysis*, second ed., Wiley-Interscience Publication, New York, 1984.

[14] B.R. Jorgensen, Y.C. Shin, Dynamics of machine tool spindle/bearing systems under thermal growth, *Journal of Tribology* 119 (1997) 875–882.

[15] S.P. Timoshenko, J.N. Goodier, *Theory of Elasticity*, third ed., McGraw-Hill, New York, 1987.

[16] R.R. Craig Jr., *Structural Dynamics*, Wiley, New York, 1981.

[17] J.M. Dickens, K.V. Pool, Modal truncation vectors and periodic time domain analysis applied to a cyclic symmetry structure, *Computers and Structures* 45 (1992) 685–696.

[18] J.M. Dickens, J.M. Nakagawa, M.J. Wittbrodt, A critique of mode acceleration and modal truncation augmentation methods for modal response analysis, *Computers and Structures* 62 (1997) 985–998.

[19] J.N. Reddy, *An Introduction To The Finite Element Method*, McGraw-Hill International Ed., New York, 1993.